Article

Climate extremes likely to drive land mammal extinction during next supercontinent assembly

Check for updates

Alexander Farnsworth [1,2] ✉, Y. T. Eunice Lo [1], Paul J. Valdes [1], Jonathan R. Buzan[3,4], Benjamin J. W. Mills[5], Andrew S. Merdith [5], Christopher R. Scotese[6] & Hannah R. Wakeford [7]

Mammals have dominated Earth for approximately 55 Myr thanks to their adaptations and resilience to warming and cooling during the Cenozoic. All life will eventually perish in a runaway greenhouse once absorbed solar radiation exceeds the emission of thermal radiation in several billions of years. However, conditions rendering the Earth naturally inhospitable to mammals may develop sooner because of long-term processes linked to plate tectonics (short-term perturbations are not considered here). In ~250 Myr, all continents will converge to form Earth's next supercontinent, Pangea Ultima. A natural consequence of the creation and decay of Pangea Ultima will be extremes in p_{CO_2} due to changes in volcanic rifting and outgassing. Here we show that increased p_{CO_2}, solar energy ($F_\odot$; approximately +2.5% W m^{-2} greater than today) and continentality (larger range in temperatures away from the ocean) lead to increasing warming hostile to mammalian life. We assess their impact on mammalian physiological limits (dry bulb, wet bulb and Humidex heat stress indicators) as well as a planetary habitability index. Given mammals' continued survival, predicted background p_{CO_2} levels of 410–816 ppm combined with increased $F_\odot$ will probably lead to a climate tipping point and their mass extinction. The results also highlight how global landmass configuration, p_{CO_2} and $F_\odot$ play a critical role in planetary habitability.

Anthropogenic emissions of greenhouse gasses are pushing Earth's climate towards a warmer state not seen for millions of years[1], with repercussions for ecosystem resilience. Yet, it is unknown whether or when Earth's dominant terrestrial animal species, mammals, will ever reach a climatic tipping point whereby their ascendancy is threatened. Sherwood and Huber[2] have suggested that current global warming will

raise temperatures above terrestrial mammalian physiological limits, rendering some parts of the world uninhabitable. Mid-to-late century International Panel on Climate Change Sixth Assessment Report[3,4] high-emission scenarios suggest that some physiological thermal thresholds will be exceeded in small, mainly coastal, regions of Africa, Australia, Europe and South Asia[5,6]. Even with the combustion of all

[1]School of Geographical Sciences and Cabot Institute for the Environment, University of Bristol, Bristol, UK. [2]State Key Laboratory of Tibetan Plateau Earth System, Environment and Resources (TPESER), Institute of Tibetan Plateau Research, Chinese Academy of Sciences, Beijing, China. [3]Climate and Environmental Physics, University of Bern, Bern, Switzerland. [4]Oeschger Centre Climate Change Researcher, University of Bern, Bern, Switzerland. [5]School of Earth and Environment, University of Leeds, Leeds, UK. [6]Department of Earth and Planetary Science, Northwestern University, Evanston, IL, USA. [7]School of Physics, HH Wills Physics Laboratory, University of Bristol, Bristol, UK. ✉e-mail: alex.farnsworth@bristol.ac.uk

available fossil fuels (+12 °C by 2300), most of the land surface would still be habitable[2]. What is certain is that the Earth will leave the Sun's habitable zone in several billion years[7] when solar luminosity ($F_\odot$; W m^{-2}) reaches a point where radiative heating and moist processes initiate a runaway greenhouse. However, conditions that threaten mammalian predominance on Earth may naturally arise sooner.

Mammalian lineage (including endothermic vertebrates belonging to the class Mammalia of the phylum Chordata) first emerged ~310 million years ago (Ma)[8] but only became the dominant species after the Cretaceous–Palaeogene (K–Pg) extinction[9]. Mammals' success has seen habitation of nearly every terrestrial biome, encompassing periods of large climatic fluctuations and mass extinctions, showing resilience to climate change[10,11]. Mammalian physiology has evolved to remove excess heat through thermoregulatory mechanisms (sweat glands, locomotion and circulatory system) owing to an ancestral legacy having evolved under warmer, non-glaciated climates[12]. Although mammals are resilient to temperature fluctuations, thermal tolerances are invariant across latitudes, elevation and phylogeny[12], showing that physiological constraints exist where survivability is limited. Sustained dry-bulb temperatures (T_d) of >40 °C can lead to mortality[12,13]. Hyperthermia, a further upper limit, occurs when the ambient wet-bulb temperature (T_w) exceeds approximately 35 °C, because the transfer of metabolic heat through sweat-based latent cooling is insufficient[2,13–16]. Exposure above this threshold for >6 h leads to death[13,17], but this threshold is rarely reached in our current climate[14]. Humidex, another heat stress measure, is a unitless indicator based on dry-bulb temperature and vapour pressure that is used by the Meteorological Service of Canada to represent human thermal comfort in hot, dry continental interiors[18]. Values of ≥30 indicate 'some discomfort', ≥45 is 'dangerous' and prolonged exposure will lead to heat stroke, while ≥54 indicates heat stroke and imminent mortality. There is a divergence between heat stress metrics where hyperthermia can be induced. T_w heat stress has a greater impact on tropical hot and humid regimes[2,17], whereas Humidex better represents dry, hot climates like deserts[18], such as those found in the continental interiors. Habitability is constrained not just by a warming climate but also by a cooling climate. Hypothermia can arise as a direct consequence of cold temperatures. Prolonged exposure to wind chill temperatures below −10 °C (T_{frost}) causes ischaemic necrosis on exposed skin. However, a more relevant measure of habitability for mammals is temperatures below freezing (T_0), which affects freshwater availability and induces plant dormancy (<5 °C; ref. 19). The planetary habitability index (PHI)[20] also offers another measure to assess mammalian survivability on the basis of constructing indices from a star–planet distance, star temperature and the wavelengths of light absorbed by a planetary body[21] to assess thermal tolerances.

The next supercontinent, Pangea Ultima (PU)[22] (Fig. 1 and Supplementary Fig. 1), is predicted to form in the next ~250 Myr (ref. 23). By ~250 Myr our Sun will emit ~2.5% more energy compared with today (~1% per 110 Myr (ref. 24) in $F_\odot$), a radiative forcing +5.55 W m^{-2} (more than double present-day p_{CO_2} (3.7 W m^{-2})). Coupled with tectonic–geographic variations in atmospheric p_{CO_2} and enhanced continentality effect for supercontinents[25], Earth could reach a tipping point rendering it uninhabitable to mammalian life.

Predicting future p_{CO_2} in ~250 Myr is challenging. The geologic record has shown large swings in p_{CO_2} (ref. 26) over the past 3.5 billion years. However, there is an apparent cool–warm in-phase relationship (for example, the Rodinia and Gondwana supercontinents) as part of the natural cycle (~400–600 Myr) of assembly, tenure and break-up of supercontinents with p_{CO_2}. However, this is complicated and depends on mechanical and insulating effects of continents on mantle convection[27] (for example, the Nuna Supercontinent stayed warm throughout the assembly–decay). This is a result of competing factors that modulate CO_2 sources and sinks (volcanic outgassing versus silicate weathering) of the long-term carbon cycle[27–29]. There have been at least five

periods of tectonic convergent cycles that have resulted in continental assembly[30] coinciding with large variations in global temperature[31]. Relatively little is known about the p_{CO_2} and climate conditions of the first four supercontinents (Vaalbara approximately 3,600–2,800 Ma, Kenorland approximately 2500 Ma, Nuna approximately 1,800–1,300 Ma and Rodinia approximately 1,100–600 Ma), although during the Snowball Earth events (approximately 720–650 Ma), p_{CO_2} is believed to have built-up to two or three orders of magnitude greater than present-day values[32,33]. More is known about the most recent supercontinent, Gondwana, approximately 550–170 Ma (also including Pangea 330–170 Ma). During the time of the Gondwanan Supercontinent, atmospheric p_{CO_2} varied from ~200 ppm (reconstructions vary between 96–435 ppm) at ~334 Ma to ~2,100 ppm (1,127–2,909 ppm) at ~255 Ma (ref. 34). This led to periods of extremes in temperature from panglacial climates during the Carboniferous (−5 °C compared with the present-day global mean[35,36]) to greenhouse climates of the Devonian (+10 °C compared with the present-day global mean[37]), all periods where $F_\odot$ was weaker (<-3%; ref. 38) than today. It has been suggested that, once a supercontinent has assembled, the rate of Large Igneous Province (LIP) emplacement increases, raising p_{CO_2}. This process can initiate continental break-up[39], leading to increased continental rifting and a further injection of p_{CO_2} (ref. 40).

Will the formation and decay of the PU Supercontinent lead to Earth becoming uninhabitable for mammals by surpassing their thermal physiological limitations long before $F_\odot$ becomes high enough to cause a runaway greenhouse? In this Article, we assess the impact of mammalian thermal tolerances resulting from numerical simulations at 0, 70, 140, 280, 560 and 1,120 ppm p_{CO_2}, under both modern and future $F_\odot$ (1,364.95 and 1,399.07 W m^{-2}). We employ a version of the United Kingdom Met Office Hadley Centre Coupled Model (HadCM3L) a dynamic fully coupled atmosphere-land-ocean general circulation model (GCM) with an interactive ozone scheme under a PU geography (see Methods for details). Further, we utilize the spatial-continuous integration (SCION) biogeochemistry model in conjunction with these simulations to quantitatively estimate background atmospheric carbon dioxide concentrations to predict how much of the land surface remains habitable by 250 Myr.

Results
PU mammalian thermal tolerance
PU grid-weighted global mean annual temperature (GMAT) ranges from 19.9 to 27.3 °C (land-only GMAT ranges from 24.5 to 35.1 °C) (0–1,120 ppm CO_2; +2.5% Modern $F_\odot$) (Fig. 1 and Table 1). The GMAT anomaly relative to the Pre-industrial control simulation (280 ppm p_{CO_2}; modern $F_\odot$) for PU varies between +8.2 and +16.1 °C (land-only GMAT anomalies range between +12.2 and +29.8 °C). When changing only the global geography (280 ppm; Modern $F_\odot$) from its Pre-industrial configuration to PU, GMAT warms by +3.5 °C, while land-only temperatures increase by +13.9 °C as a result of the continentality effect.

When the mammalian physiological metrics T_d (Extended Data Fig. 1), T_w (Extended Data Fig. 2), Humidex (Extended Data Fig. 3), T_0 and T_{frost} are applied to all scenarios, they present varying amounts of mammalian habitation (Extended Data Fig. 4). Here, we define habitability (Table 1) by exceeding conditions where: (1) cold monthly mean temperature >0 °C (T_0) for at least three consecutive months, (2) T_w < 34.5 °C and (3) $T_{Humidex}$ < 45.

Hibernation is encoded in these metrics. Hibernation is an effective strategy for mammals in times of cold stress once sufficient fat stores have been built up. This is required as plants (food) enter dormancy once temperatures are <5 °C (ref. 19). Using a more conservative estimate of <0 °C also removes freshwater availability. Aestivation, that is, warm weather dormancy, cannot occur in regions where plants cannot grow, usually in hot, arid regions. Subsequently, we also rule out desert regions as habitable (low species diversity; Fig. 1a) owing to low water and food availability. To ensure that the model shows skill,
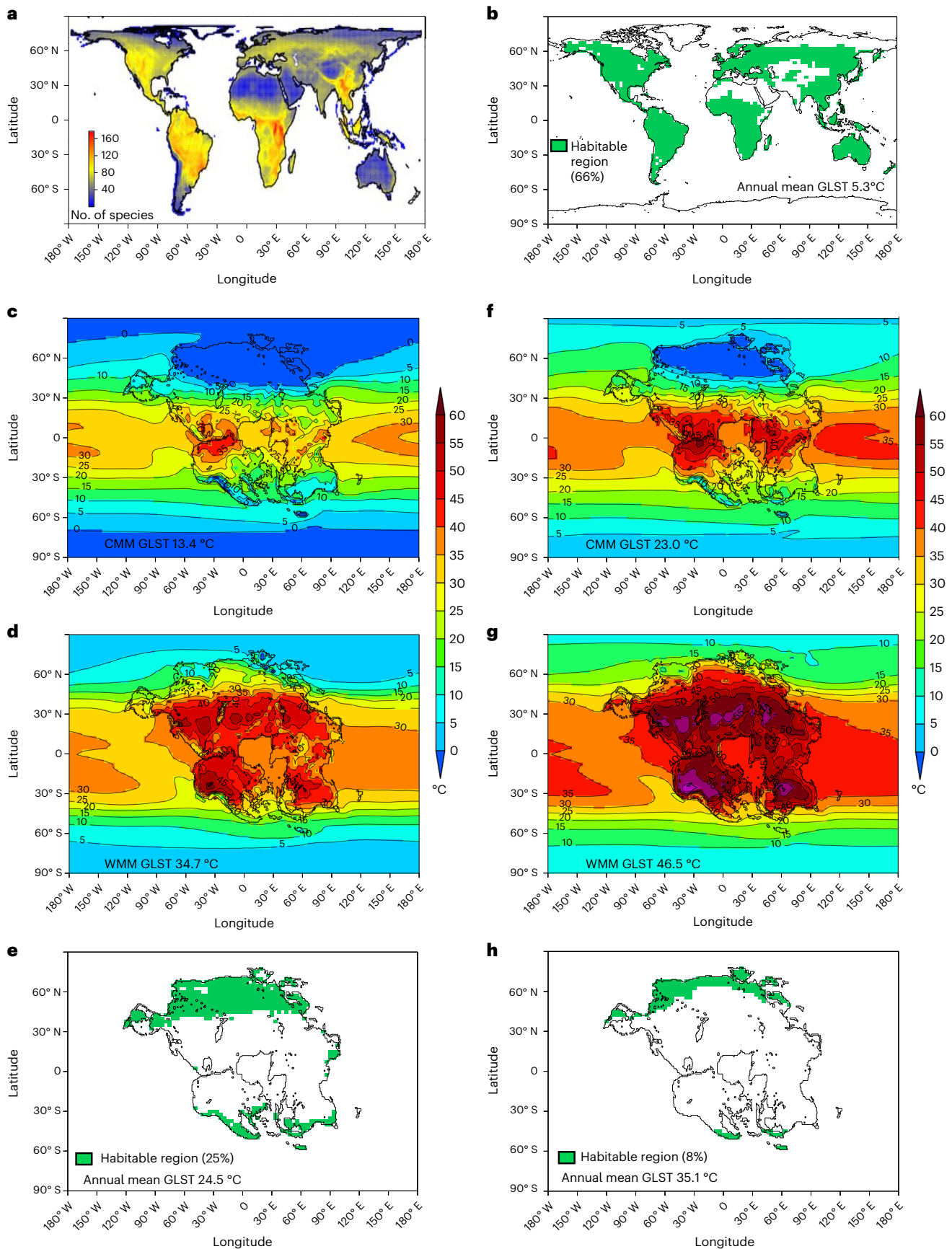
Fig. 1 | PU temperature and habitability. a, Mammalian species diversity without the influence of humans (reproduced from ref. 41). **b**, Habitable regions (green area) in the Pre-industrial simulation. **c**–**h**, Cold month mean temperature (CMMT; °C) (**c**,**f**), warm month mean temperature (WMMT; °C) (**d**,**g**) and

habitable regions (green area) (**e**,**h**) under two end members of our sensitivity analysis: low-p_{CO_2} conditions (280 ppm) PU planetary configuration (+250 Ma) (**c**–**e**) and high-p_{CO_2} conditions (1,120 ppm) PU configuration (+250 Ma) (**f**–**h**), with global land surface temperature (GLST) (grid-weighted) indicated.

Table 1 | Pre-industrial and PU climate simulations for a range of CO_2 (ppm) and solar luminosities (Sol), both Modern and in 250 Myr (Sol+2.5%); see Table 2 in Methods for details

	Habitability metrics							
Scenario	Carbon dioxide concentration (ppm)	Habitable land (million km²)	Habitable land (million km²)	Percentage of total habitable land	Desert percentage of planet	Land and ocean (°C)	Land only (°C)	ΔT_{eq} (°C)
Pre-industrial	280	147.9	97.5	66%	30%	11.73	5.32	3.7[a]
PU, 280 ppm, Sol	280	145.5	78.8	54%	42%	15.28	19.22	2.4
PU, 560 ppm, Sol	560	145.5	39.8	27%	40%	19.28	23.97	4.0
PU, 1,120 ppm, Sol	1,120	145.5	24.9	17%	40%	22.59	28.64	3.3
PU, 280 ppm, Sol+2.5%	280	145.5	36.0	25%	44%	19.89	24.53	2.3
PU, 560 ppm, Sol+2.5%	560	145.5	23.8	16%	47%	23.36	29.28	3.5
PU, 1,120 ppm, Sol+2.5%	1,120	145.5	12.0	8%	49%	27.30	35.12	3.9
PU, 560 ppm, Sol+2.5%, 2×Orog	560	145.5	27.3	19%	43%	21.75	24.78	1.9

Total land area (km²) and habitable land area (km² and %; see Methods for details) for each experiment are shown for habitability metrics. The percentage of land area that is desertified is also indicated. Grid-weighted global mean annual and land-only mean annual temperatures along with global equilibrium climate sensitivity (ΔT_{eq}) are highlighted. 'Orog' signifies orography. [a]From ref. 62.

Table 2 | Description of sensitivity studies and model boundary conditions for a Pre-industrial climate (Modern geography) and PU geography

Scenario	Experiment name	Time (Myr)	pCO_2 (ppm)	$F_{\odot}$ (W m⁻²)	Geography	Modification to geography
Pre-industrial	xmxxc	0	280	1,364.95	Modern	No
PU, 0 ppm, Sol	teurk	~250	0	1,364.95	PU	No
PU, 70 ppm, Sol	teurl	~250	70	1,364.95	PU	No
PU, 140 ppm, Sol	teurm	~250	140	1,364.95	PU	No
PU, 280 ppm, Sol	teurc	~250	280	1,364.95	PU	No
PU, 560 ppm, Sol	teurd	~250	560	1,364.95	PU	No
PU, 1,120 ppm, Sol	teure	~250	1,120	1,364.95	PU	No
PU, 0 ppm, Sol+2.5%	teurr	~250	0	1,399.07	PU	No
PU, 70 ppm, Sol+2.5%	teurs	~250	70	1,399.07	PU	No
PU, 140 ppm, Sol+2.5%	teurt	~250	140	1,399.07	PU	No
PU, 280 ppm, Sol+2.5%	teurg	~250	280	1,399.07	PU	No
PU, 560 ppm, Sol+2.5%	teurh	~250	560	1,399.07	PU	No
PU, 1,120 ppm, Sol+2.5%	teuri	~250	1,120	1,399.07	PU	No
PU, 560 ppm, Sol+2.5%, 2×Orog	teurp	~250	560	1.399.07	PU	Topographic height doubled

CO_2, solar constant and any modifications made are detailed for each experiment.

we evaluated our Pre-industrial control simulation against Modern observed mammalian species distribution where the impact of humans has been removed[41], showing good agreement (Fig. 1).

Only one scenario (280 ppm p_{CO_2}; Table 1) has comparable amounts of habitable land (54%) to the Pre-Industrial Earth (66%) under increased future $F_{\odot}$. Under 560 or 1,120 ppm, habitability decreases to 16% and 8%, respectively. In all cases, increasing p_{CO_2} pushes the majority of the land surface beyond thermal physiological tolerances for T_d, T_w and Humidex (Fig. 1), and at 1,120 ppm the planet is practically uninhabitable (8% habitability). Even if the land surface height is doubled, habitability increases only marginally from 16% to 19% at 560 ppm (Table 1). Although silicate weathering feedbacks have the potential to draw down p_{CO_2} to extremely low levels, leading to climates where cold thermal tolerances are exceeded and extinction occurs, such a scenario is less plausible under future $F_{\odot}$ (ref. 42), As such, scenarios

(Table 1) and analysis where p_{CO_2} is low (140, 70 and 0 ppm) are only discussed in 'Cold Stress Environments' in Supplementary Information.

PU energy balance analysis

Energy balance analysis[43] (Extended Data Figs. 5 and 6d) indicates that, changing from Pre-industrial geography to a PU geography (280 ppm CO_2, Modern $F_{\odot}$ kept constant to remove its influence) leads to an increase in GMAT of +3.7 °C (Extended Data Fig. 5a) driven by changes in surface albedo (+2.2 °C) and emissivity (+1.4 °C) at high latitudes owing to there being no polar ice (mainly though ice and cloud feedbacks). The addition of future $F_{\odot}$ (+2.5% $F_{\odot}$) increases GMAT by +8.2 °C (Extended Data Fig. 5d). A fraction (+1.8 °C) of this increase is directly attributable to increased $F_{\odot}$ and indirectly through changes in albedo (+2.7 °C), emissivity (+3.7 °C) and heat transport (+0.1 °C) as a result
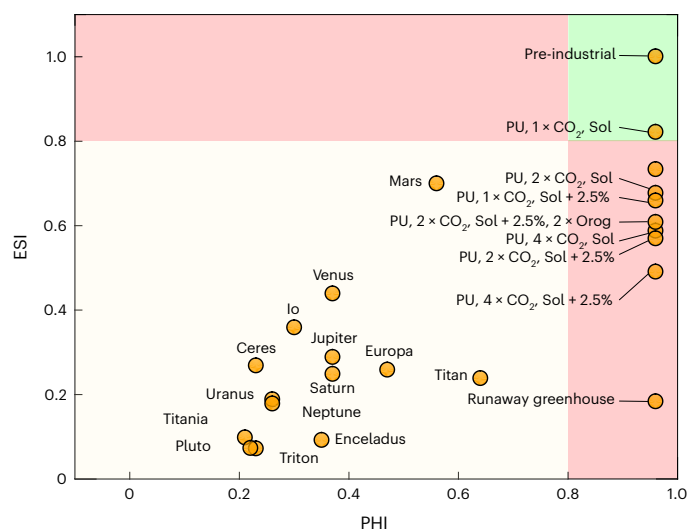
Fig. 2 | Astrophysical habitability index. ESI and PHI of all Solar System bodies and each PU p_{CO_2} and solar luminosity (Modern (Sol) and solar luminosity in 250 Myr (Sol + 2.5%)) sensitivity study (orange symbols). Values within the green zone indicate habitability (see Methods for details). Values in the red zone indicate poor habitability due to having a rocky interior (high PHI) but not a temperate surface (low ESI) and vice versa. See ref. 20 for ESI and PHI for definitions and planetary body values for the Solar System.

of non-linear feedbacks that arise from increasing $F_\odot$. This is driven by a reduction in seasonal sea ice at high latitudes (compare Extended Data Fig. 5a,d), whereas just increasing p_{CO_2} impacts GMAT predominantly through emissivity-driven feedbacks (Extended Data Fig. 5a–c). Terrestrial albedo changes are primarily driven by vegetation feedbacks due to desertification under warming conditions (Table 1) that are already enhanced because of supercontinent formation with no p_{CO_2} or $F_\odot$ change (30–42%). When $F_\odot$ is kept at Pre-industrial levels, deserts show a small decrease with increasing p_{CO_2} owing to increased evaporation and moisture enrichment of the atmosphere, leading to an invigorated hydrological cycle in some regions (Table 1).

A stepwise doubling of p_{CO_2} under $F_\odot$ (+2.5%) from 280 to 1,120 ppm (Extended Data Fig. 6d–f) shows a general increase in equilibrium climate sensitivity (ΔT_{eq} of 2.3–3.9 °C; Table 1). Interestingly, ΔT_{eq} analysis of the same suite of p_{CO_2} concentrations but with a modern $F_\odot$ (Table 1) indicates more variable ΔT_{eq} with p_{CO_2} (ΔT_{eq} of 2.4–4.8 °C), demonstrating non-linear climate feedbacks with changes in $F_\odot$.

Finally, we consider an astrophysical classification of PHI in conjunction with an Earth Similarity Index (ESI) based on planetary mass, radius, temperature, stable substrate, available energy, chemistry and ability to host liquid water[20]. These are defined relative to the only known habitable planet, Earth, and habitability is defined as greater than 0.8 (see online methods for further details). Hence, by definition, the only parameter that changes in the future is GMAT, since all other factors remain constant. According to the ESI, no future scenario is predicted to remain habitable (Fig. 2).

PU p_{CO_2} modelling
Continent–continent collision during supercontinent formation, on average, is predicted to reduce, not increase, p_{CO_2} drawdown because high topography (and more readily erodible material) is concentrated in the dry continental interiors, away from moisture sources[27]. Moisture pathways may be just as important as topography in influencing chemical weathering. This is corroborated in our model, which sees a reduction both in precipitation (Extended Data Fig. 7) and in runoff when only changing the continental configuration from a Pre-industrial world to a PU world. Increasing p_{CO_2} reduces precipitation and runoff

into the continental interior, theoretically further reducing chemical weathering and increasing p_{CO_2}.

To better constrain the likely p_{CO_2} and understand the silicate weathering feedback in our PU reconstruction, we use the global climate–biogeochemical model SCION (see Methods for more information), which computes the long-term carbon cycle and uses a two-dimensional (2D) terrestrial weathering module informed by climate model simulations. Here, a data structure of climate model outputs at different CO_2 levels is used to simulate spatial continental processes through variations in atmospheric CO_2, and we update this with the climate model runs from this study both for the Pre-industrial (which determines the initial steady state) and for PU. To run the model, we must also prescribe the tectonic rate of CO_2 degassing, which we estimate from a conservative set of plate boundaries (mid-ocean ridges and subduction zones) that might describe the gross tectonic fabric of the PU world (see Supplementary Information for more details). We find that PU is likely to have 1.3–1.9 times the degassing rate of the present-day Earth, which is roughly equivalent to the rates proposed for Pangea[44]. SCION ensemble simulations for PU predict a mean long-term background p_{CO_2} of 621 ppm (range 410–816 ppm) when considering the range of uncertainty in the degassing rate as well as the potential for changing reactivity of global silicate rocks.

Discussion
The formation and decay of PU will limit and, given a much greater source-to-sink ratio of p_{CO_2}, ultimately end terrestrial mammalian habitability on Earth by exceeding their warm thermal tolerances, billions of years earlier than previously hypothesized. Inevitable changes in both plate tectonics and $F_\odot$ create feedbacks in the climate, even in lieu of variable p_{CO_2}, that will raise GMAT.

Further, tectonic evolution of PU will lead to large variations in p_{CO_2} (over 10^2 years (for example, hyperthermal events[45]) and 10^5 years (for example, volcanism[46])), as observed through the geologic record and seen as a natural consequence of supercontinent assembly and decay[27], enhancing GMAT (20.9–24.8 °C at 410–816 ppm p_{CO_2}). Further, the tenure of PU possibly increases the likelihood of massive hyperthermal events akin to the Permian–Triassic event that saw up to 10 °C warming on 10^4 year time scales[45].

Today, critical heat stress measures are rarely exceeded on land and, if so, only for short time scales[14] (hours or days). If only the geography was to change, critical heat stress is not exceeded but does drive the climate towards critical thresholds (Fig. 1 and Extended Data Figs. 1–3). Combined with a future increase in $F_\odot$, large regions of the supercontinent breach these critical thresholds for periods of >30 days (Table 1, Fig. 1 and Extended Data Fig. 4). At 280 ppm, most of the Tropics become uninhabitable, and by 1,120 ppm this extends through the mid to high latitudes. Although the high latitudes (>50°) at 1,120 ppm offer limited refugia from critical heat stress, cold stress metrics further reduce habitability (Extended Data Fig. 4). Only highly specialized migratory mammals would be able to compete. However, even a migratory strategy may be perilous for mammals owing to continent-wide deserts and aridity (Table 1) throughout PU acting as a biogeographic barrier (Extended Data Fig. 7). High T_d and T_w as a function of increasing p_{CO_2} require plentiful water availability for mammals to balance losses through evaporative cooling to stop hyperthermia. Rates of evaporative water loss will increase with hyperthermia as the rate of respiratory water loss increases in direct proportion to increases in the rate of gas exchange[47], making traversing these near 50° N to 50° S continent-wide arid and desert regions impractical. A secondary impact of low moisture availability would be an increase in the vapour pressure deficit (VPD) and plant stress (not shown) and a reduction in the productivity and food availability of vegetated land for mammals. Under 1,120 ppm p_{CO_2}, the VPD between 50° N and 50° S is a factor of three or four greater than in the Gobi Desert today (with our

Pre-industrial model showing similar values of approximately 10–12 hPa compared with observations[48]).

Hibernation (a seasonal adaptation to prolonged periods of food shortage and cold) and its hot weather equivalent, aestivation, have been effective strategies for mammals for millions of years to combat relative extremes in temperatures. Today, ~50% of mammals hibernate[49], and of those, only a small fraction for more than 1 month[50]. With p_{CO_2} predicted to be 410–816 ppm, cold stress will be less of a constraint on mammalian habitability (Extended Data Fig. 4). Burrows and cave systems, which are buffered from external air temperature, may allow some refugia for some mammal species if food and water are plentiful. Small burrowing rodents may show greater survivorship in regions above thermal thresholds if staying active at night rather than during the day. However, even if increasing the aestivation period is allowed from 1–3 months during the warmest months of the year, habitability is only marginally increased (Supplementary Table 2) at 280, 560 and 1,120 ppm from 25% 16% and 8% to 32%, 21% and 13%, respectively, as a result of adjoining months being above physiological thresholds.

Although we cannot discount evolutionary adaptation to heat and cold stress, recent studies have shown that mammalian thermotolerance upper limits are conserved through geologic time[12,51] and have not increased during past rapid (for example, Palaeocene–Eocene Thermal Maximum) or slower warming events (Early–Eocene Climatic Optimum). Mammalian physiological limitations show that increasing their upper thermal tolerance is a slow process (0.6 °C per Myr) with an upper T_d boundary of approximately 40 °C that is rarely crossed. At 40–60 °C, plant life and the basis of the terrestrial food chain begins to critically fail owing to damage to photosystem II, leading to decreased electron transport rates and photosynthetic failure[12,52]. At ≥560 ppm, daily $T_d > 40$ °C are consistent throughout the supercontinent (at 1,120 ppm, this can often reach >50–60 °C). Although mammals are better at adapting to cold tolerance[12,51], a more conservative ≤0 °C threshold whereby freshwater sources are rendered biologically unavailable offers a finite lower thermal tolerance limit. To adapt to more humid and warmer environments, endotherms would need to increase body temperature (T_b) above both the dry- and/or wet-bulb temperature (T_a) to maintain a negative $T_b - T_a$ gradient. However, since most endotherms regulate T_b near lethal or physiological limits, there is probably only limited scope for thermal adaptation[16]. This is likely conservative given that juvenile mammals will be more susceptible to lower ranges[53].

Over long-time scales (10^6 years), weathering feedbacks will regulate p_{CO_2} owing to higher $F_\odot$ increasing surface temperatures and enhancing the long-term hydrological cycle, thereby reducing p_{CO_2}. However, weathering feedbacks will have a lagged response[28], operating on longer time scales than are important for mammalian habitability, meaning that any substantial p_{CO_2} outgassing would lead to short-term (10^3–10^4 year) warming that would reduce habitability through heat stress, such as during supercontinent assembly that has consistently been shown to result in high p_{CO_2} emissions (1,000–3,000 ppm)[54] (see Methods for more details).

Reduced moisture advection (Extended Data Fig. 1) into continental interiors leads to large arid regions where surface runoff is reduced or non-existent (not shown). This reduces the carbon sink (via both chemical weathering and biotic factors), raising p_{CO_2} through a reduction in terrestrial p_{CO_2} sequestration, erosion and transport of carbon for oceanic sequestration[55].

In PU, a Tropical east–west trending mountain range (Supplementary Fig. 1) is modelled, from which an invigorated hydrologic cycle is derived, driven from the mountain range proximity to oceanic moisture. Consequently, we speculate a moistened atmosphere from greenhouse conditions, and a strong land–sea contrast would progressively increase silicate weathering, drawing down p_{CO_2}. When the topography of PU is doubled in height, the hydrological cycle decreases over the higher mountains (Extended Data Fig. 7), suggesting that silicate

weathering and p_{CO_2} drawdown may slow. On the other hand, if the erodible material of these mountain ranges was made of sedimentary material with low silica content, it would instead release large amounts of p_{CO_2} through the oxidation of rock-rich inorganic carbon and sulfide minerals[56], increasing p_{CO_2} further and expanding regions where mammals would experience critical heat stress.

Today critical cold stress (T_{frost} or T_0) environments are limited to the high to mid latitudes (>30°). Changing geography and increased $F_\odot$ both shift this zone at least 10° towards the poles. Cold stress is still a factor limiting habitability regardless of changing geography and increased $F_\odot$, which both act to warm the planet. Elevated p_{CO_2} (>1,120 ppm) effectively removes all cold stress environments. Cool-adapted mammals that have lower thermal physiological limits will be particularly impacted by rising temperatures as well as increased competition from other species moving poleward as they migrate away from the Tropics.

Other future supercontinent configurations have been proposed (Novopangea, Aurica and Amasia[23,57]). All formations except Amasia suggest a supercontinent landmass centred in the Tropics and would likely lead to climates similar to PU. Amasia, however, would be centred over the North Pole (except for Antarctica, which remains in its present-day position). In such a scenario, under a range of p_{CO_2} regimes, large regions would probably be less affected by critical heat stress and remain habitable. However, strong weathering feedbacks under such a scenario may present greater challenges from cold stress on mammalian physiology. Ice–albedo feedbacks may also present a situation where Amasia[57] would glaciate more readily, even under higher p_{CO_2} regimes and mass extinction.

Ultimately, it is supercontinent geography and increased $F_\odot$ that drive the increased sensitivity to variable p_{CO_2}. Continued mammalian habitability will be contingent on no large, sustained, pulses of p_{CO_2}, either through processes in supercontinent assembly and decay or coincident outgassing events (for example, LIPs such as the Siberian or Deccan traps), both of which have precedent throughout the geologic record. Elevated p_{CO_2} levels (>840 ppm), often associated with greenhouse climates, have been common over most of the Phanerozoic[26,58]. If p_{CO_2} was to spike ≥560 ppm, even for a short period (10^2–10^3 years), Earth will become inhospitable for mammalian life, resulting in a mass extinction comparable to the 'Big 5' extinction events[59]. This may even be conservative. Song et al.[60] suggest that warming of >5.2 °C from Pre-industrial levels led to previous mass extinctions in marine animals[60], and their defined threshold is passed under scenarios below 280 ppm p_{CO_2}.

This analysis pinpoints the importance of tectonics, atmospheric constituents and solar energy for continued mammalian survivability. Under all scenarios of an 'Earth-like' planet, regions of habitability do exist (even for 1,120 ppm p_{CO_2}, $F_\odot$ +2.5%, albeit small (Extended Data Fig. 4)). However, no future realization of PU where p_{CO_2} is ≥280 ppm passes a well-used astrophysical assessment of habitability (Fig. 2), meaning that Earth will leave its astrophysical defined habitable zone (at least temporarily) well before a runaway greenhouse occurs. This suggests that the potential for human habitability of many exoplanets might be mistakenly discounted. This is illustrated by the recent discovery of KOI-456.04 (ref. 61), which has an Earth–Sun system similar to our own and an estimated GMAT of 5 °C. The habitability of KOI-456.04 may be more dependent on the position of its continental landmass and concentration of atmospheric constituents than an arbitrary habitable zone defined by planet–star distance.

Online content

Any methods, additional references, Nature Portfolio reporting summaries, source data, extended data, supplementary information, acknowledgements, peer review information; details of author contributions and competing interests; and statements of data and code availability are available at https://doi.org/10.1038/s41561-023-01259-3.

References

1. Tierney, J. et al. Past climates inform our future. *Science* **370**, 680–692 (2020).
2. Sherwood, S. C. & Huber, M. An adaptability limit to climate change due to heat stress. *Proc. Natl Acad. Sci. USA* **107**, 9552–9555 (2010).
3. Ranasinghe, R. et al. in *Climate Change 2021: The Physical Science Basis* Ch. 12 (eds Masson-Delmotte, V. et al.) 1767–1926 (IPCC, Cambridge Univ. Press, 2021).
4. IPCC *Climate Change 2021: The Physical Science Basis* (eds Masson-Delmotte, V. et al.) (Cambridge Univ. Press, 2021).
5. Im, E. S., Pal, J. S. & Eltahir, E. A. B. Deadly heat waves projected in the densely populated agricultural regions of South Asia. *Sci. Adv.* **3**, e1603322 (2017).
6. Pal, J. S. & Eltahir, E. A. B. Future temperature in southwest Asia projected to exceed a threshold for human adaptability. *Nat. Clim. Change* **6**, 197–200 (2016).
7. Wolf, E. T., Shields, A. L., Kopparapu, R. K., Haqq-Misra, J. & Toon, O. B. Constraints on climate and habitability for Earth-like exoplanets determined from a general circulation model. *Astrophys. J.* **837**, 107 (2017).
8. Rowe, T. B. *The Emergence of Mammals* Vol. 2, 1–52 (Elsevier, 2017).
9. Chiarenza, A. A. et al. Asteroid impact, not volcanism, caused the end-Cretaceous dinosaur extinction. *Proc. Natl Acad. Sci. USA* **117**, 17084–17093 (2020).
10. Bininda-Emonds, O. R. P. et al. The delayed rise of present-day mammals. *Nature* **446**, 507–512 (2007).
11. Petryshyn, V. A. et al. The role of temperature in the initiation of the end-Triassic mass extinction. *Earth Sci. Rev.* **208**, 103266 (2020).
12. Bennett, J. M. et al. The evolution of critical thermal limits of life on Earth. *Nat. Commun.* **12**, 1198 (2021).
13. Asseng, S., Spankuch, D., Hernandez-Ochoa, I. M. & Laporta, J. The upper temperature thresholds of life. *Lancet Planet Health* **5**, E378–E385 (2021).
14. Raymond, C., Matthews, T. & Horton, R. M. The emergence of heat and humidity too severe for human tolerance. *Sci. Adv.* **6**, eaaw1838 (2020).
15. Nowack, J., Levesque, D. L., Reher, S. & Dausmann, K. H. Variable climates lead to varying phenotypes: 'weird' mammalian torpor and lessons from non-Holarctic species. *Front. Ecol. Evol.* https://doi.org/10.3389/fevo.2020.00060 (2020).
16. Boyles, J. G., Seebacher, F., Smit, B. & McKechnie, A. E. Adaptive thermoregulation in endotherms may alter responses to climate change. *Integr. Comp. Biol.* **51**, 676–690 (2011).
17. Buzan, J. Ra. H. & Moist, M. Heat stress on a hotter Earth. *Annu. Rev. Earth Planet. Sci.* **48**, 623–655 (2020).
18. Sobolewski, A., Mlynarczyk, M., Konarska, M. & Bugajska, J. The influence of air humidity on human heat stress in a hot environment. *Int. J. Occup. Saf. Ergon.* **27**, 226–236 (2021).
19. Rabenhorst, M. Biologic zero: a soil temperature concept. *Wetlands* **25**, 616–621 (2005).
20. Schulze-Makuch, D. et al. A two-tiered approach to assessing the habitability of exoplanets. *Astrobiology* **11**, 1041–1052 (2011).
21. Bryson, S. et al. The occurrence of rocky habitable-zone planets around solar-like stars from Kepler data. *Astron. J.* **161**, 36 (2021).
22. Scotese, C. R. & Wright, N. PALEOMAP Paleodigital Elevation MOdels (PaleoDEMS) for the Phanerozoic, PALEOMAP Project. *EarthByte* https://www.earthbyte.org/paleodem-resource-scotese-and-wright-2018/ (2018).
23. Davies, H. S., Green, J. A. M. & Duarte, J. C. Back to the future: testing different scenarios for the next supercontinent gathering. *Glob. Planet. Change* **169**, 133–144 (2018).
24. Wolf, E. T. & Toon, O. B. Delayed onset of runaway and moist greenhouse climates for Earth. *Geophys. Res. Lett.* **41**, 167–172 (2014).
25. Tabor, N. P. & Poulsen, C. J. Palaeoclimate across the Late Pennsylvanian–Early Permian tropical palaeolatitudes: a review of climate indicators, their distribution, and relation to palaeophysiographic climate factors. *Palaeogeogr. Palaeoclimatol. Palaeoecol.* **268**, 293–310 (2013).
26. Foster, G. L., Royer, D. L. & Lunt, D. J. Future climate forcing potentially without precedent in the last 420 million years. *Nat. Commun.* **8**, 14845 (2017).
27. Jellineck, A., Lenardic, A. & Pierrehumbert, R. Ice, fire, or fizzle: the climate footprint of Earth's supercontinental cycles. *Geochem. Geophys. Geosyst.* **21**, 1–45 (2020).
28. Gernon, T. M. et al. Global chemical weathering dominated by continental arcs since the mid-Palaeozoic. *Nat. Geosci.* **14**, 690–696 (2021).
29. McKenzie, N. R. et al. Continental arc volcanism as the principal driver of icehouse–greenhouse variability. *Science* **352**, 444–447 (2016).
30. Bradley, D. C. Secular trends in the geologic record and the supercontinent cycle. *Earth Sci. Rev.* **108**, 16–33 (2011).
31. Haywood, A. et al. What can palaeoclimate modelling do for you? *Earth Syst. Environ.* **3**, 1–18 (2019).
32. Pierrehumbert, R. T. High levels of atmospheric carbon dioxide necessary for the termination of global glaciation. *Nature* **429**, 646–649 (2004).
33. Gernon, T. M., Hincks, T. K., Tyrrell, T., Rohling, E. J. & Palmer, M. R. Snowball Earth ocean chemistry driven by extensive ridge volcanism during Rodinia breakup. *Nat. Geosci.* **9**, 242–U283 (2016).
34. Anagnostou, E. et al. Changing atmospheric CO_2 concentration was the primary driver of early Cenozoic climate. *Nature* **533**, 380–384 (2016).
35. Hoffman, P. F. et al. Snowball earth climate dynamics and cryogenian geology-geobiology. *Sci. Adv.* **3**, e1600983 (2017).
36. Voigt, A., Abbot, D., Pierrehumbert, R. & Marotzke, J. Initiation of a Marinoan Snowball Earth in a state-of-the-art atmosphere–ocean general circulation model. *Climate* **7**, 249–263 (2011).
37. Mills, B. J. W. et al. Modelling the long-term carbon cycle, atmospheric CO_2, and Earth surface temperature from late Neoproterozoic to present day. *Gondwana Res.* **67**, 172–186 (2019).
38. Gough, D. O. Solar interior structure and luminosity variations. *Sol. Phys.* **74**, 21–34 (1981).
39. Heron, P. J. Mantle plumes and mantle dynamics in the Wilson cycle. *Geol. Soc. Lond. Spec. Publ.* **470**, 87–103 (2019).
40. Brune, S., Williams, S. E. & Muller, R. D. Potential links between continental rifting, CO_2 degassing and climate change through time. *Nat. Geosci.* **10**, 941–946 (2017).
41. Faurby, S. & Svenning, J. C. Historic and prehistoric human-driven extinctions have reshaped global mammal diversity patterns. *Divers Distrib.* **21**, 1155–1166 (2015).
42. Feulner, G., Bukenberger, M. & Petri, S. Tracing the Snowball bifurcation of aquaplanets through time reveals a fundamental shift in critical-state dynamics. *Earth Syst. Dynam* **14**, 533–547 (2023).
43. Heinemann, M., Jungclaus, J. H. & Marotzke, J. Warm Paleocene/Eocene climate as simulated in ECHAM5/MPI-OM. *Climate* **5**, 785–802 (2009).
44. Marcilly, C. M., Torsvik, T. H., Domeier, M. & Royer, D. L. New paleogeographic and degassing parameters for long-term carbon cycle models. *Gondwana Res.* **97**, 176–203 (2021).
45. Hu, X., Li, J., Han, Z. & Li, Y. Two types of hyperthermal events in the Mesozoic–Cenozoic: environmental impacts, biotic effects, and driving mechanisms. *Sci. China Earth Sci.* **63**, 1041–1058 (2020).

46. Wignall, P. The link between large igneous province eruptions and mass extinctions. *Elements* **1**, 293–297 (2005).

47. Lovegrove, B. G. et al. Are tropical small mammals physiologically vulnerable to arrhenius effects and climate change? *Physiol. Biochem. Zool.* **87**, 30–45 (2014).

48. Zhang, H. M., Wu, B. F., Yan, N. N., Zhu, W. W. & Feng, X. L. An improved satellite-based approach for estimating vapor pressure deficit from MODIS data. *J. Geophys. Res. Atmos.* **119**, 12256–12271 (2014).

49. Turbill, C., Bieber, C. & Ruf, T. Hibernation is associated with increased survival and the evolution of slow life histories among mammals. *Proc. R. Soc. B* **278**, 3355–3363 (2011).

50. Geiser, F. Aestivation in mammals and birds. *Prog. Mol. Subcell. Biol.* **49**, 95–111 (2010).

51. Araujo, M. B. et al. Heat freezes niche evolution. *Ecol. Lett.* **16**, 1206–1219 (2013).

52. Feeley, K. *et al*. The thermal tolerances, distributions, and performances of tropical montane tree species. *Front. Glob. Chang.* https://doi.org/10.3389/ffgc.2020.00025 (2020).

53. Laburn, H. P., Mitchell, D. & Goelst, K. Fetal and maternal body temperatures measured by radiotelemetry in near-term sheep during thermal-stress. *J. Appl. Physiol.* **72**, 894–900 (1992).

54. Godderis, Y. et al. Onset and ending of the late Palaeozoic ice age triggered by tectonically paced rock weathering. *Nat. Geosci.* **10**, 382–386 (2017).

55. Godderis, Y., Donnadieu, Y., Le Hir, G., Lefebvre, V. & Nardin, E. The role of palaeogeography in the Phanerozoic history of atmospheric CO_2 and climate. *Earth Sci. Rev.* **128**, 122–138 (2014).

56. Hilton, R. G. & West, A. J. Mountains, erosion and the carbon cycle. *Nat. Rev. Earth Environ.* **1**, 284–299 (2020).

57. Way, M., Davies, H. S., Duarte, J. C. & Green, M. The climates of Earth's next supercontinent: effects of tectonics, rotation rate, and insolation. *Geochem. Geophy. Geosy.* **22**, e2021GC009983 (2021).

58. Witkowski, C. R. et al. Validation of carbon isotope fractionation in algal lipids as a p_{CO_2} proxy using a natural CO_2 seep (Shikine Island, Japan). *Biogeosciences* **16**, 4451–4461 (2019).

59. Raup, D. M. & Sepkoski, J. J. Mass extinctions in the marine fossil record. *Science* **215**, 1501–1503 (1982).

60. Song, H. et al. Thresholds of temperature change for mass extinctions. *Nat. Commun.* **12**, 4694 (2021).

61. Heller, R. et al. Transit least-squares survey: III. A 1.9 R-circle plus transit candidate in the habitable zone of Kepler-160 and a nontransiting planet characterized by transit-timing variations. *Astron. Astrophys.* **638**, A10 (2020).

62. Farnsworth, A. et al. Climate sensitivity on geological timescales controlled by nonlinear feedbacks and ocean circulation. *Geophys. Res. Lett.* **46**, 9880–9889 (2019).

Methods

Numerical modelling framework

An overview of the model setup, boundary conditions, sensitivity studies and carbon dioxide modelling is given below.

Model. Here, we utilize the HadCM3LB-M2.1aD[63] GCM, a member of the UK Meteorological Office HadCM3 family of climate models[64]. The grid resolution is 3.75° × 2.5° in longitude × latitude in both the atmosphere (19 vertical levels) and ocean (20 vertical levels), employing the Arakawa B-grid scheme.

Ocean salinity is adjusted to an ice-free world global mean reference value of 34.23 practical salinity units and allowed to freely evolve globally. To prevent millennial-scale salinity drift during model spin-up, the total ocean volume integral is calculated and is re-adjusted to back to ice-free world global mean after each ocean time step. Sea-ice coverage is calculated from a zero-layer model overlaying the top-most layer of the ocean grid. Sea ice forms using a threshold value of −1.8 °C, with albedo set at 0.8 for temperatures below −10 °C and 0.5 for temperatures above 0 °C, with a linear variation between.

Parameterizations include the radiation scheme of Edwards and Slingo[65], the convection scheme of Gregory et al.[66] and the Met Office Surface Exchange Scheme (MOSES)-2.1 land-surface scheme, whose representation of evaporation includes the dependence of stomatal resistance on temperature, vapour pressure and CO_2 concentration[67]. There are nine sub-grid-scale land surface types, four non-vegetated types (urban, lakes, bare soil, ice and inland water), and five plant functional types (broadleaf trees, needleleaf trees, shrubs, C3 (temperate) grasses and C4 (tropical) grasses), updated every 10 model days.

The Top-Down Representation of Interactive Foliage and Flora Including Dynamics (TRIFFID) dynamic vegetation model[67] is employed, allowing two-way coupled interactions between the land surface and atmosphere. The MOSES 2.1 land surface scheme was employed, as opposed to MOSES 2.2, owing to the former producing a better representation of Pre-industrial climates in combination with the TRIFFID model[68] as well as because the future distribution of vegetation needs to be predicted based on the simulated climate. Crucially, TRIFFID allows full interaction between climate and feedbacks associated with vegetation cover and complex land surface–atmosphere interactions.

Desert soil albedo is interactively updated on the basis of the soil carbon content, where low soil carbon concentrations result in a modified soil albedo of 0.32 (average modern-day Saharan albedo).

Typically, the ozone distribution is prescribed as a static latitude–pressure–time distribution in many climate models. However, in warmer climates of the past or future, the tropopause rises, meaning that stratospheric ozone penetrates into the troposphere[69], which is unphysical if a Pre-industrial tropopause height is prescribed for warm time periods. Instead, the ozone distribution is prescribed using a dynamic approach[70] in which ozone is dynamically coupled to the model tropopause height with constant values for the troposphere (0.02 ppm), tropopause (0.2 ppm) and stratosphere (5.5 ppm). This change makes a negligible difference to the global mean surface temperature but does have a small impact on the stratospheric temperature and winds.

HadCM3LB-M2.1aD, part of the United Kingdom Met Office HadCM3 family of climate models, has been extensively evaluated against modern-day observations as part of the International Panel on Climate Change Climate Model Intercomparison Project phase 5, showing good skill in reproducing a climate that is comparable to observations as well as other higher-fidelity climate models[63]. A full description of the individual sub-component models in HadCM3LB-M2.1aD is given in ref. 63.

Boundary conditions and initialization. The reconstruction of tectonics, structures and plate motion that underpin this study is based on a +250 Myr reconstruction of PU[22]. This reconstruction uses methods similar to those of Valdes and Markwick[71], where land–sea mask, bathymetric, topographic and the sub-grid-scale orographic variables are required by the model and are interpolated onto the GCM resolution (Supplementary Fig. 1). There are no assumed terrestrial ice sheets in this reconstruction. Shorelines in this reconstruction represent the maximum transgression in sea level assuming that no terrestrial ice sheets are present. PU is only one of four potential configurations (three of which are similar in continental distribution with a supercontinent centred in the Tropics[23]) of supercontinent formation by 250 Myr.

All simulations are initialized from an equilibrated Pre-industrial state (atmosphere and ocean).

Modern $F_\odot$ is set at 1,364.95 W m^{-2}. $F_\odot$ increases by -1% per 110 Myr (ref. 38). We forecast an $F_\odot$ of 1,399.07 W m^{-2} (+2.5% increase from Modern) by 250 Myr. Although modern solar luminosity has recently been revised to 1,361 W m^{-2}, the model has been calibrated for the previous value of 1,364.95 W m^{-2}. For all simulations conducted, we use a Modern orbital configuration. A set of sensitivity studies to constrain the impact of atmospheric carbon dioxide are conducted at 70, 140, 280, 560 and 1,120 ppm. Table 1 gives an overview of the sensitivity studies conducted in this study.

Simulations are run for 5,000 model years and reached equilibrium at both the surface (not strongly trending, less than 0.1 °C per century in the global mean) and deep ocean, with less than 0.3 W m^{-2} imbalance in the top-of-atmosphere net radiation. Long model integrations are required when running new configurations to ensure that ocean circulation is fully representative of the new model boundary conditions applied to the model. The exception was the 0 ppm p_{CO_2} simulations at both 1,364.95 and 1,399.07 W m^{-2} solar luminosity. Each simulation ran for 550 and 700 model years, respectively. This is common where climate models using low p_{CO_2} values become fully glaciated (complete sea-ice coverage).

Heat and cold stress indicators

Two heat stress indicators are used within this study: (1) the wet-bulb temperature and (2) Humidex, calculated as follows:

Wet-bulb temperature. Wet-bulb temperature (T_w) is derived from a more accurate computation from ref. 72 (their equation (3.8)) with equivalent potential temperature (θ_E) calculated from ref. 73 (their equation (38)). Wet-bulb approximations such as that of Stull[74] are not desirable for use as it is calibrated for the modern day and does not apply to warmer time periods. The complete derivation can be found in appendix A of ref. 75. T_w values of ≥35 °C are assessed to be critically lethal and lead to mortality[2,13,17].

Humidex index. Humidex is a measure of the combined effect of both temperature and humidity on human physiology. Although a more subjective metric and often equated to a simplified feels-like metric, it does have an upper limit of 54. Above this limit for 6 h, mortality will ensue through heat stroke as the body is unable to regulate its core body temperature (T_b) through evaporation at the skin surface. Humidex is calculated as

$$\text{Humidex} = T + 0.5555 \times \left(6.11 \times e^{5417.7530 \times \left(\frac{1}{273.15} - \frac{1}{273.15 - T_{dew}} \right)} - 10 \right), \quad (2)$$

where T is air temperature (°C) and T_{dew} is the dew-point temperature (K)[76]. Here, we define a region as uninhabitable where the monthly mean Humidex value of ≥45 for acclimatized species, which is defined as dangerous by the Meteorological Service of Canada, where all activity should be stopped. Using mean monthly values is conservative given that daily maximum Humidex values will exceed this value consistently.

Warm stress: aestivation. Of mammals that hibernate, only a small proportion do so owing to warm weather conditions, and of those, only a small proportion aestivate (warm weather hibernation) for

several hours to days[15], of which an even smaller proportion do so on seasonal time scales. Hibernation helps cold climate survivorship more than warm weather. From an ecological point of view, aestivation results in different challenges and requirements compared with hibernation in winter; while heat can reduce access to food and water availability as well, it will also reduce access to refugia for low ambient temperature (T_a) for a substantial reduction of body temperature (T_b)[50]. High T_a prevents T_b from falling to low levels and will therefore limit the energy-conserving potential of aestivation as a viable solution[50]. This is compounded by mammals' high metabolic rates that require an intake of large amounts of food, and when food supply is low or fluctuating, energy requirements may exceed energy availability. In response, here we take regions that are desert (as predicted by the dynamic interactive vegetation scheme TRIFFID) in the model and deem them uninhabitable owing to a lack of food (bare soil fraction >0.5 corresponds to uninhabitable).

Cold stress: hibernation. Today, approximately 50% of mammals hibernate[49], and mainly for days or weeks[50]. Only a fraction can do so on seasonal time scales, with only one known mammal able to do so for 11 months of the year. Here, we take a very unlikely conservative approach with our simulations and allow all mammals to develop hibernation as a trait and to hibernate for 9 months to survive cold weather conditions. We define cold stress regions that inhibit mammal habitation where nine or more consecutive months fall below 0 °C. This threshold limits freshwater availability as well as placing plants into a state of dormancy (<5 °C; ref. 19).

Exoplanet similarity index

Exoplanet habitability assessments are commonly used quantitative measures of planetary habitability. Here, we use a weighted ESI[20] that measures habitability in relation to present-day Earth. A value of between 1 (identical similarity) and 0 (no similarity) signifies the likelihood that a planet would have the same physical properties as Earth (for example, radius, mass and surface temperature). In this instance, the only changing parameter will be the global mean annual temperature, as the physical properties of Earth will not have changed in +250 Myr. Values of ≥0.8 indicate the potential to harbour life.

$$\text{ESI}(S, R) = 1 - \sqrt{\frac{1}{2}\left[\left(\frac{S - S_\oplus}{S + S_\oplus}\right)^2 + \left(\frac{R - R_\oplus}{R + R_\oplus}\right)^2\right]},$$

where S is stellar flux, R is the radius, $S_\oplus$ is Earth's solar flux and $R_\oplus$ is Earth's radius.

ESI provides the physical properties of an exoplanet's habitability but cannot explicitly measure the possibility of life. Here, we couple ESI with the PHI in a geometric mean of separate values that would constitute conditions applicable to life:

$$\text{PHI} = (S \times E \times C \times L)^{1/4},$$

where S is the presence of a stable substrate (influenced by solid subsurface, atmosphere and magnetosphere), E is the availability of energy (influenced by light, heat, redox chemistry and tidal flexing), C is appropriate chemistry (influenced by polymetric chemistry) to support life and L is a liquid solvent (in either the atmosphere or the sub-surface). While values for S, E, C and L are difficult to exactly determine on exoplanets, for our purposes here these are known values with respect to Earth. See ref. 20 for further details.

$$\text{PHI}_\text{rel} = (\text{PHI}/\text{PHI}_\text{max}).$$

Each parameter (S, E, C, L) is summed and divided by the maximum attainable value to normalize the score (PHI_rel) to between 0 and 1.

Here, we define values of ≥0.8 as giving a reasonable approximation of conditions that allow life. A value of 1.0 would constitute 'maximum' habitability. Today, Earth has a value of 0.96. See ref. 20 for further details.

Future p_{CO_2} modelling

To quantitatively estimate the long-term stable atmospheric CO_2 concentration during PU, we use the SCION earth evolution model[77]. SCION is a linked climate–biogeochemical model that estimates a self-consistent evolution of the major composition of Earth's atmosphere and oceans over geological time. It is an extension of the popular Geologic Carbon-Cycle[78,79] and Carbon, Oxygen, Phosphorus, Sulphur and Evolution[80,81] box models that use a 2D continental surface and look-up tables of steady-state climate model outputs to approximate surface processes such as weathering. The model calculates atmospheric CO_2 based on tectonic and weathering-related CO_2 inputs, as well as carbon sequestration as organic carbon or carbonates. SCION has been tested over the Phanerozoic Eon and produces a reasonable fit to CO_2 proxy data, particularly over the last 250 Myr (ref. 77).

Using HadCM3B runs for the present day and for PU, we update the climate and palaeogeographic data structure within SCION so that it can run from the Pre-industrial to 250 Myr in the future. SCION also requires an estimate of global tectonic CO_2 degassing. This is derived from global tectonic fluxes (that is, the amount of new seafloor created at mid-ocean ridges and consumed at subduction zones) and the amount of carbon that is typically degassed from such environments. Estimates of both the flux and amount of carbon degassed are available for present day[82,83], and we use the recent estimates of ref. 82 as our present-day benchmark for carbon degassing (13 and 18 Mt C per year at ridges and subduction zones, respectively).

To estimate the carbon degassing for PU, we first construct a hypothetical plate boundary network (that is, an interconnected set of subduction zones and mid-ocean ridges[84]; Supplementary Fig. 1). The configuration is based on that which is inferred to have existed while Pangea was active (and what is mostly still visible today): a 'ring of fire' acting as an (almost) complete girdle of subduction circumnavigating PU[85–87]. For mid-ocean ridges, we infer the simplest and most conservative of all configurations, a stable triple junction that can account for convergence at all subduction zones. (A similar approach is taken for plate tectonic models in deep time[86,88].)

To determine the rate of crust being formed and consumed at ridges and subduction zones, we extracted the spreading rates of all oceanic tectonic plates that compose the Pacific Ocean since 154 Ma (the time at which we have preserved isochrons in the Pacific Ocean). We limit our analysis to just the Pacific Ocean, as it is most analogous to our PU world (that is, plates consisting just of oceanic crust that are being subducted; see the discussion in ref. 89). We find a mean spreading rate of 10.42 cm per year with a standard deviation of 1.76 cm per year (Supplementary Fig. 2). This range of 8.67–12.18 cm per year provides us with a possible estimate of mid-ocean ridge and subduction flux. We multiply and sum the fluxes by the expected carbon degassing for both present-day and PU and use the ratio of the two as the relative change in degassing. Our results suggest that PU is likely to have 1.3–1.9 times the degassing rate of present-day Earth (roughly equivalent to and in line with estimates for Pangea degassing relative to present day[44]).

Now that we have defined an assumed CO_2 degassing rate and have built a data structure of climate model runs at different CO_2 levels for 250 Myr+, we can run the SCION model forwards in time to simulate atmospheric CO_2 evolution over geological time. We start the model run at 50 Myr with all forcings fixed at present-day values. Between 0 and 250 Myr+, we increase the degassing rate linearly between 1 (present day) and the 250 Myr+ value calculated above. To account for model uncertainty, we run the system 1,000 times subject to a random choice from the range of future degassing rates, as well as the parameter space tested in the standard Phanerozoic model ensembles[77]. Supplementary

Fig. 3 shows the model spatial fields at Pre-industrial and 250 Myr+, and Supplementary Fig. 1 shows the predicted atmospheric CO_2 concentration for each of these times, with the central marker showing the model ensemble mean and the bars showing the minimum and maximum. Like Pangaea, PU has a large arid interior zone in which silicate weathering is inhibited but also a large warm and wet climate zone in which weathering is enhanced. The overall combination of higher CO_2 degassing and altered continental weatherability results in a prediction of 621 ppm (range 410–816 ppm) CO_2, or a range of approximately 1.5–3 times Pre-industrial (Table 2).

Data availability

All data needed to evaluate the conclusions in the paper are present in the paper and/or Supplementary Information. Model data can be accessed from the repository at www.bridge.bris.ac.uk/resources/simulations.

References

63. Valdes, P. J. et al. The BRIDGE HadCM3 family of climate models: HadCM3@Bristol v1.0. *Geosci. Model Dev.* **10**, 3715–3743 (2017).
64. Gordon, C. et al. The simulation of SST, sea ice extents and ocean heat transports in a version of the Hadley Centre coupled model without flux adjustments. *Clim. Dyn.* **16**, 147–168 (2000).
65. Edwards, J. & Slingo, A. Studies with a flexible new radiation code. 1. Choosing a configuration for a large-scale model. *Q. J. R. Meteorol. Soc.* **122**, 689–719 (1996).
66. Gregory, J. & Mitchell, J. The climate response to CO_2 of the Hadley Centre coupled AOGCM with and without flux adjustment. *Geophys. Res. Lett.* **24**, 1943–1946 (1997).
67. Cox, P. M. *Description of the TRIFFID Dynamic Global Vegetation Model, Technical Report* (Met Office Hadley Centre, 2000).
68. Loptson, C., Lunt, D. & Francis, J. Investigating vegetation-climate feedbacks during the early Eocene. *Climate* **10**, 419–436 (2014).
69. Lorenz, D. J. & DeWeaver, E. T. Tropopause height and zonal wind response to global warming in the IPCC scenario integrations. *J. Geophys. Res. Atmos.* https://doi.org/10.1029/2006jd008087 (2007).
70. Smith, A. K. et al. Satellite observations of high nighttime ozone at the equatorial mesopause. *J. Geophys. Res. Atmos.* https://doi.org/10.1029/2008jd010066 (2008).
71. Markwick, P. & Valdes, P. Palaeo-digital elevation models for use as boundary conditions in coupled ocean-atmo sphere GCM experiments: a Maastrichtian (late Cretaceous) example. *Palaeogeogr. Palaeoclimatol. Palaeoecol.* **213**, 37–63 (2004).
72. Davies-Jones, R. An efficient and accurate method for computing the wet-bulb temperature along pseudoadiabats. *Mon. Weather Rev.* **136**, 2764–2785 (2008).
73. Bolton, D. The computation of equivalent potential temperature. *Mon. Weather Rev.* **108**, 1046–1053 (1980).
74. Stull, R. Wet-bulb temperature from relative humidity and air temperature. *J. Appl. Meteorol. Clim.* **50**, 2267–2269 (2011).
75. Buzan, J., Oleson, K. & Huber, M. Implementation and comparison of a suite of heat stress metrics within the Community Land Model version 4.5. *Geosci. Model Dev.* **8**, 151–170 (2015).
76. Masterton, J. M. & Richardson, F. A. *Humidex, A Method of Quantifying Human Discomfort Due to Excessive Heat and Humidity* (Environment Canada, 1979).
77. Mills, B. J. W., Donnadieu, Y. & Godderis, Y. Spatial continuous integration of Phanerozoic global biogeochemistry and climate. *Gondwana Res.* **100**, 73–86 (2021).
78. Berner, R. A. A model for atmospheric CO_2 over Phanerozoic time. *Am. J. Sci.* **291**, 339–376 (1991).
79. Berner, R. A. GEOCARBSULF: a combined model for Phanerozoic atmospheric O_2 and CO_2. *Geochim. Cosmochim. Acta* **70**, 5653–5664 (2006).
80. Bergman, N. M., Lenton, T. M. & Watson, A. J. COPSE: a new model of biogeochemical cycling over Phanerozoic time. *Am. J. Sci.* **304**, 397–437 (2004).
81. Lenton, T. M., Daine, S. J. & Mills, B. J. W. COPSE reloaded: an improved model of biogeochemical cycling over Phanerozoic time. *Earth Sci. Rev.* **178**, 1–28 (2018).
82. Muller, R. D. et al. Evolution of Earth's tectonic carbon conveyor belt. *Nature* **605**, 629–639 (2022).
83. Fischer, T. P. et al. The emissions of CO_2 and other volatiles from the world's subaerial volcanoes. *Sci. Rep.* **9**, 18716 (2019).
84. Gurnis, M. et al. Plate tectonic reconstructions with continuously closing plates. *Comput. Geosci.* **38**, 35–42 (2012).
85. Collins, W. J. Slab pull, mantle convection, and Pangaean assembly and dispersal. *Earth Planet. Sci. Lett.* **205**, 225–237 (2003).
86. Domeier, M. & Torsvik, T. H. Plate tectonics in the late Paleozoic. *Geosci. Front.* **5**, 303–350 (2014).
87. Seton, M. et al. Global continental and ocean basin reconstructions since 200 Ma. *Earth Sci. Rev.* **113**, 212–270 (2012).
88. Merdith, A. S. et al. Extending full-plate tectonic models into deep time: linking the Neoproterozoic and the Phanerozoic. *Earth Sci. Rev.* **214**, 103477 (2021).
89. Merdith, A. S., Atkins, S. E. & Tetley, M. G. Tectonic controls on carbon and serpentinite storage in subducted upper oceanic lithosphere for the past 320 Ma. *Front. Earth Sci.* https://doi.org/10.3389/feart.2019.00332 (2019).

Acknowledgements

Author contributions

A.F. and P.J.V. designed the project. A.F. carried out the simulations and initial analysis, and wrote the first draft. Y.T.E.L. produced further heat stress analysis. C.S. produced the PU digital elevation model. B.J.W.M. and A.S.M. provided the SCION model data and analysis. All authors contributed to the discussion, interpretation and writing of the manuscript.

Competing interests

The authors declare no competing interests.

Additional information

Extended data is available for this paper at https://doi.org/10.1038/s41561-023-01259-3.

Supplementary information The online version contains supplementary material available at https://doi.org/10.1038/s41561-023-01259-3.

Correspondence and requests for materials should be addressed to Alexander Farnsworth.

Peer review information *Nature Geoscience* thanks Hannah Davies, Paul Mathewson and Steven Sherwood for their contribution to the peer review of this work. Primary Handling Editor: James Super, in collaboration with the *Nature Geoscience* team.

**Reprints and permissions information** is available at www.nature.com/reprints.
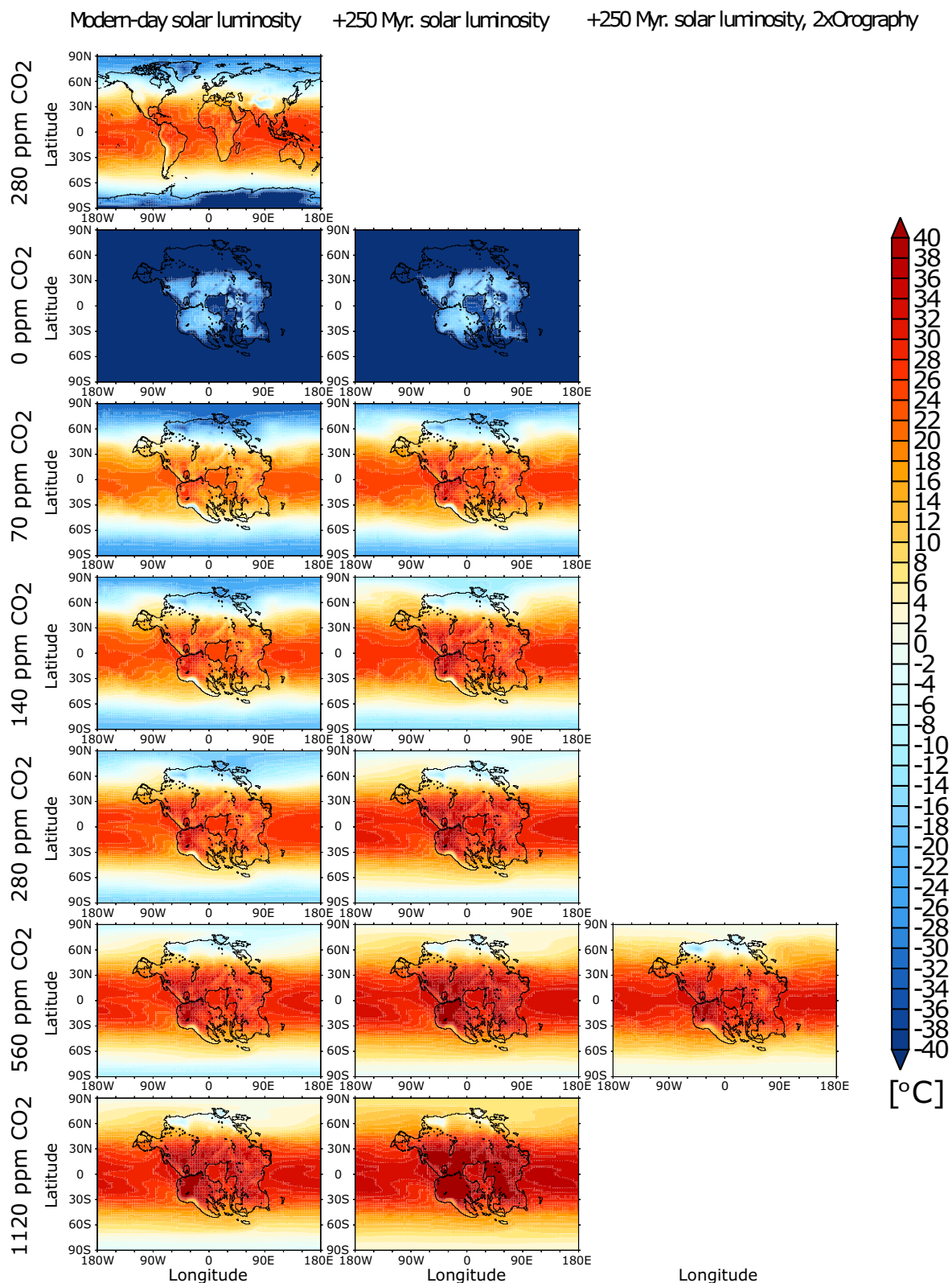
Extended Data Fig. 1 | Mean annual dry-bulb 1.5 m air temperature for each experiment. Mean annual 1.5 m air temperature C) for each experiment at present day (column 1), +2.5% present day solar luminosity (column 2) and +2.5% present day solar luminosity with a doubling of the topography (column 3) at 0 pm, 70 ppm, 140 ppm, 560 ppm and 1120 ppm CO2.
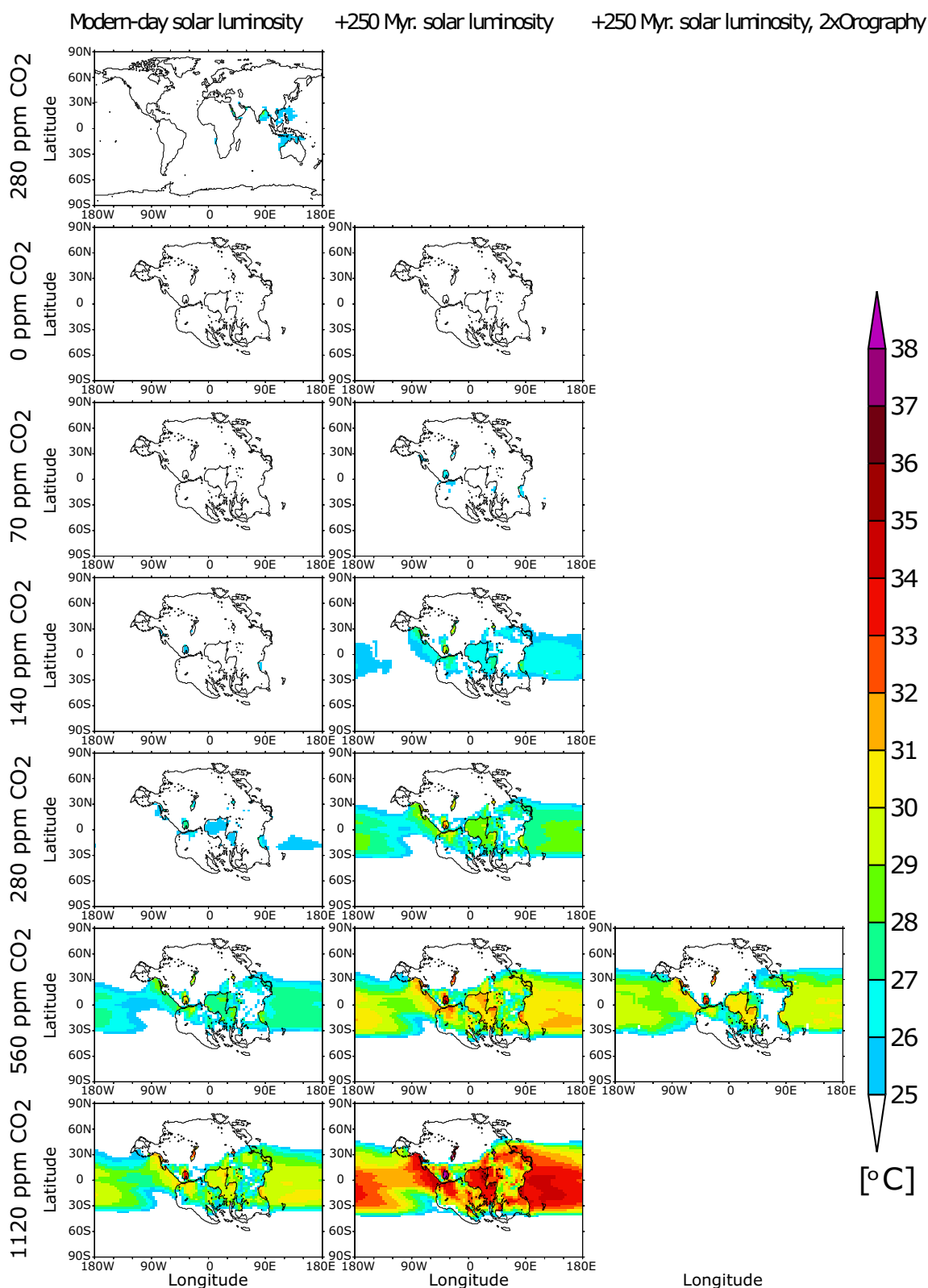
Extended Data Fig. 2 | Mean annual wet-bulb 1.5 m air temperature for each experiment. Warmest month mean 1.5 m wet-bulb temperature (°C) for each experiment at present day (column 1), +2.5% present day solar luminosity (column 2) and +2.5% present day solar luminosity with a doubling of the topography (column 3) at 0 pm, 70 ppm, 140 ppm, 560 ppm and 1120 ppm CO2.
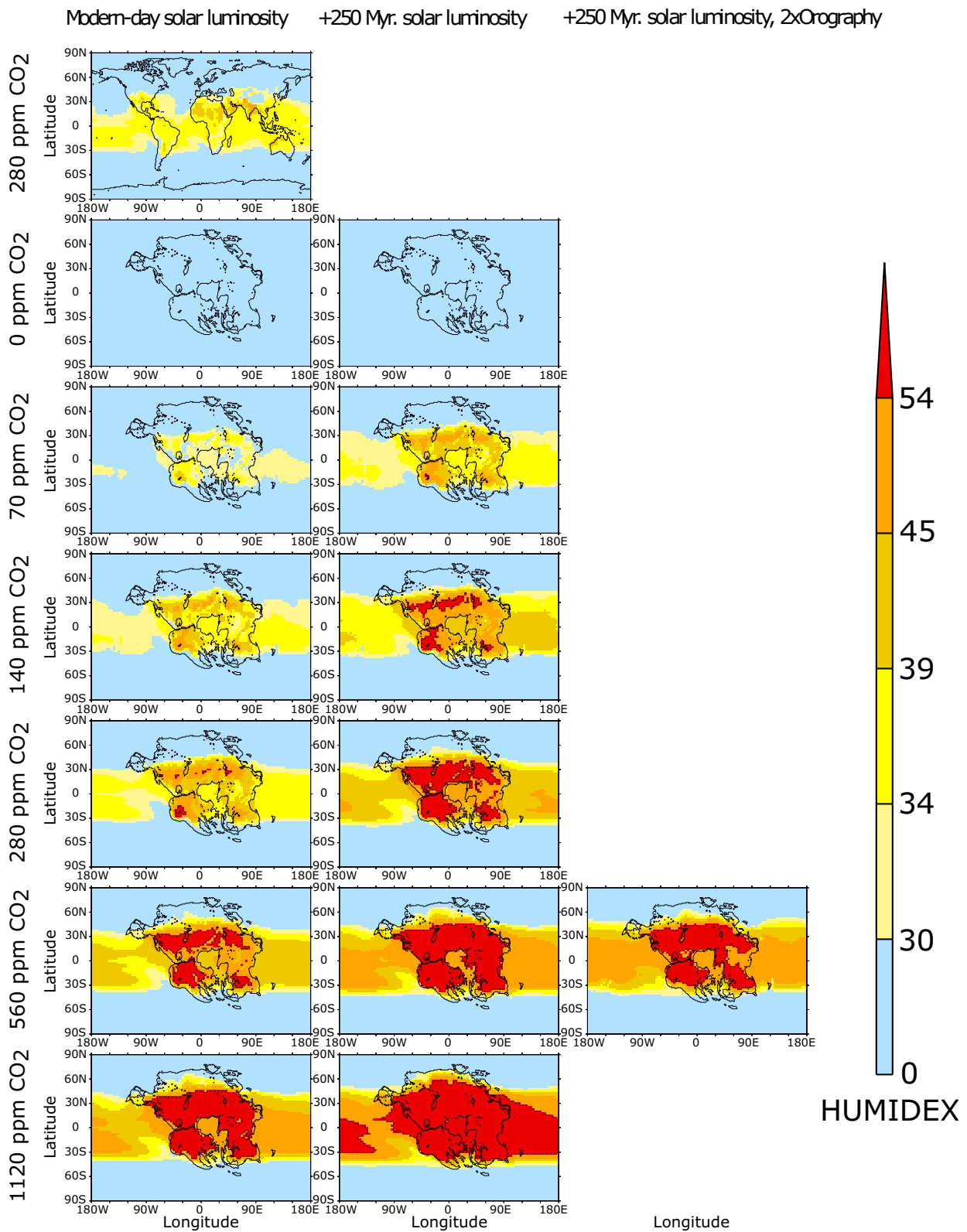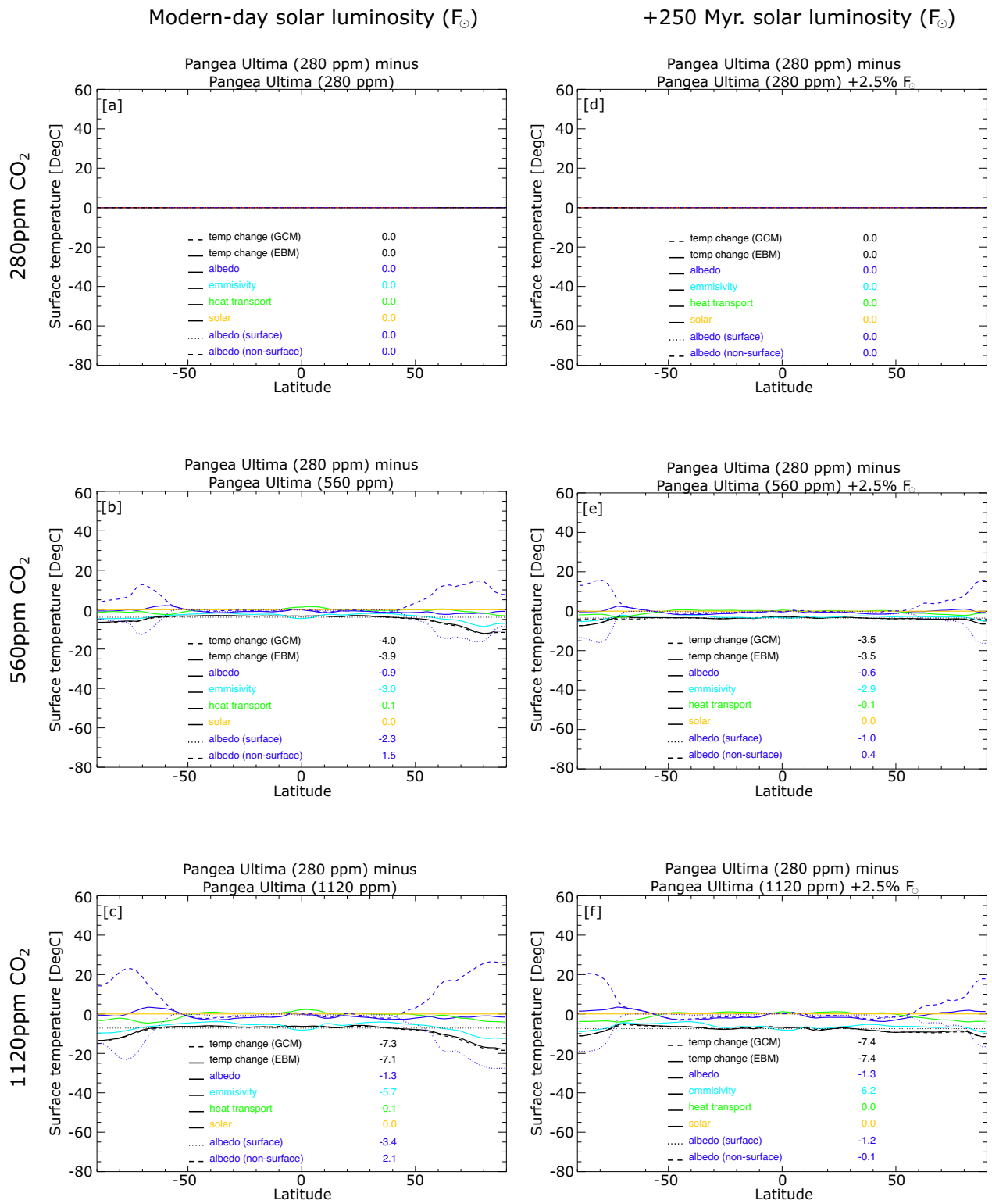
Extended Data Fig. 3 | Humidex for each experiment. Warmest month HUMIDEX for each experiment at present day (column 1), +2.5% present day solar luminosity (column 2) and +2.5% present day solar luminosity with a doubling of the topography (column 3) at 0 pm, 70 pm, 140 pm, 560 pm and 1120 pm CO2.
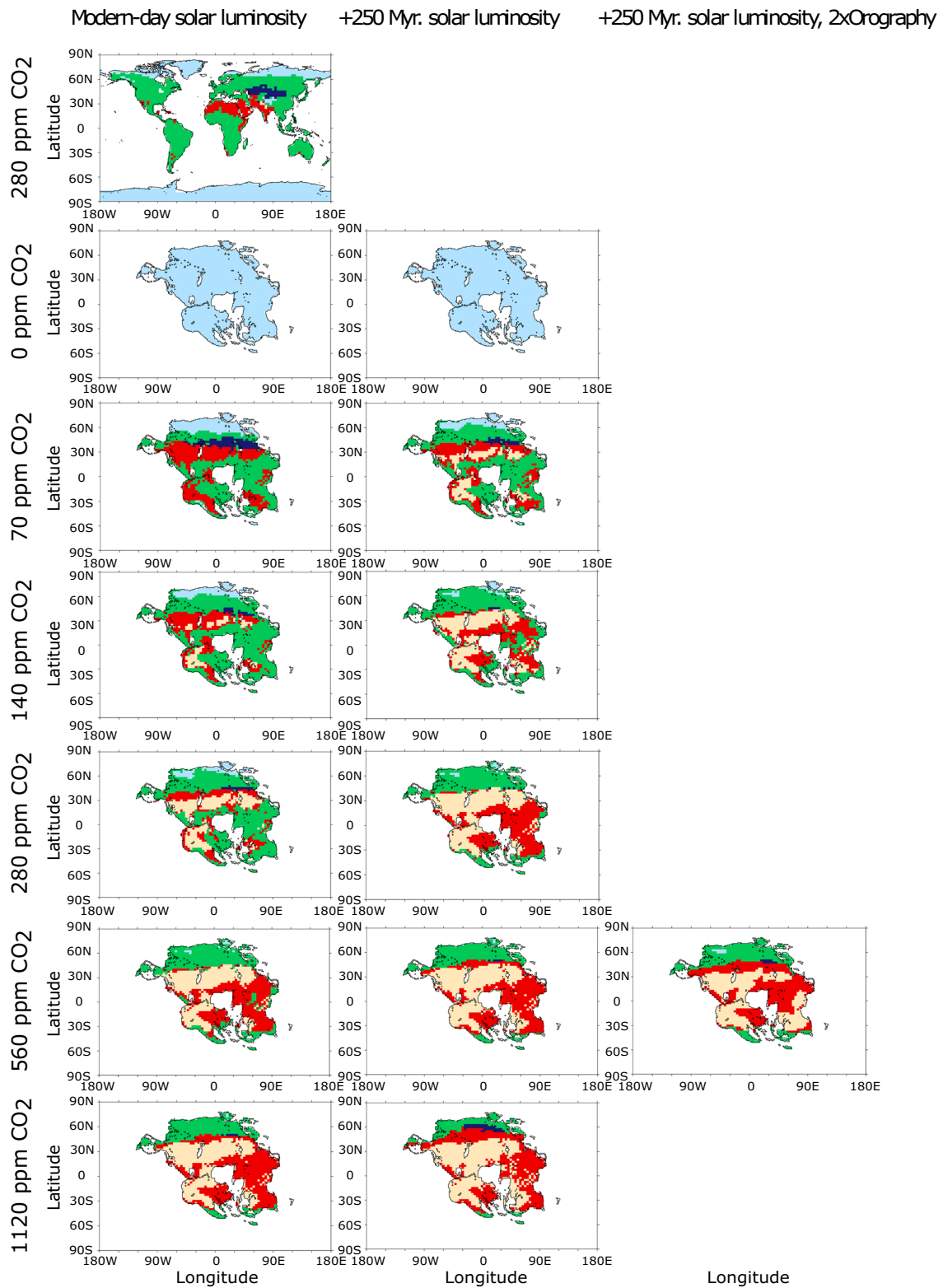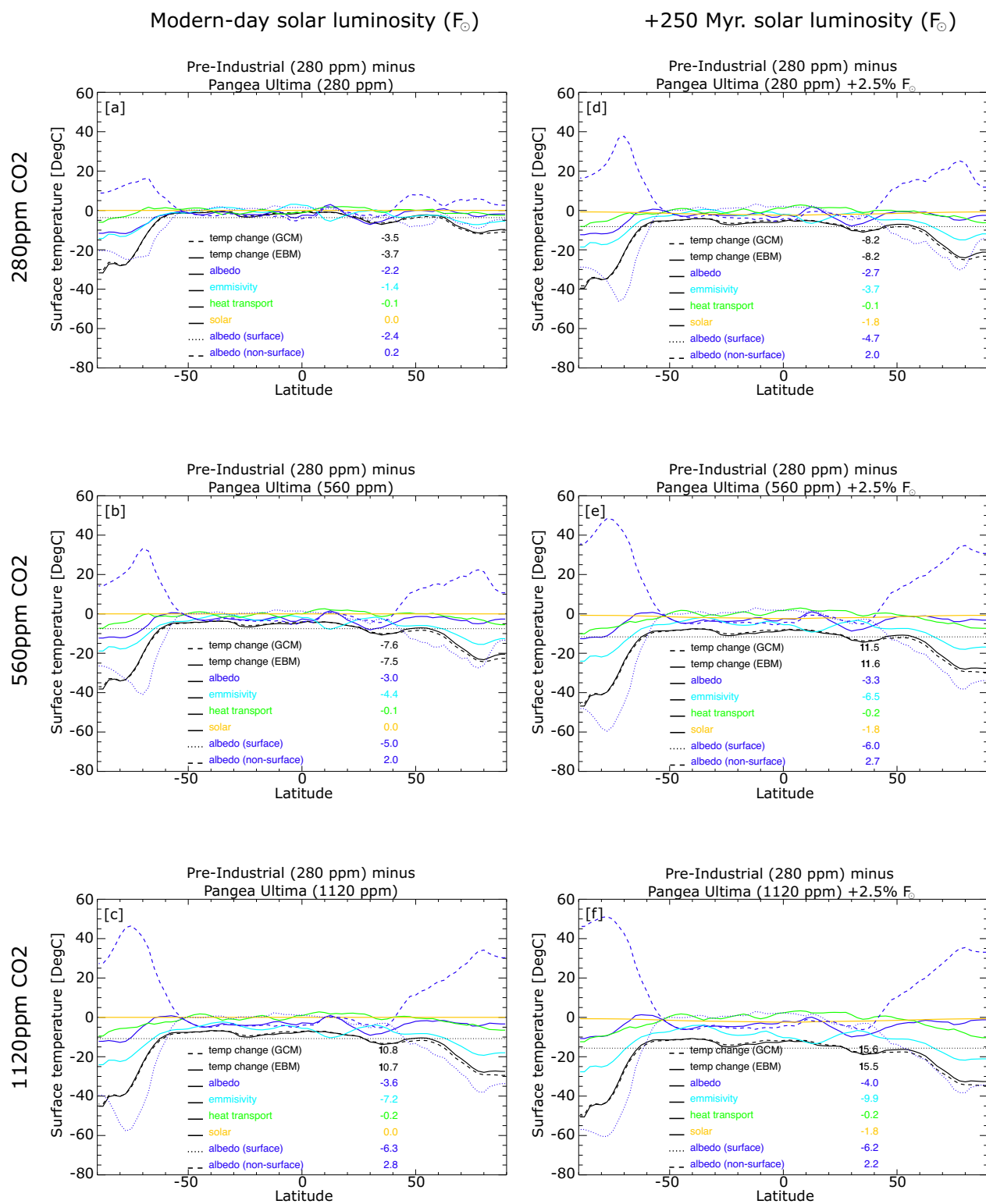
Extended Data Fig. 4 | Amount of habitable land for each experiment. Habitability for each experiment at present day (column 1), +2.5% present day solar luminosity (column 2) and +2.5% present day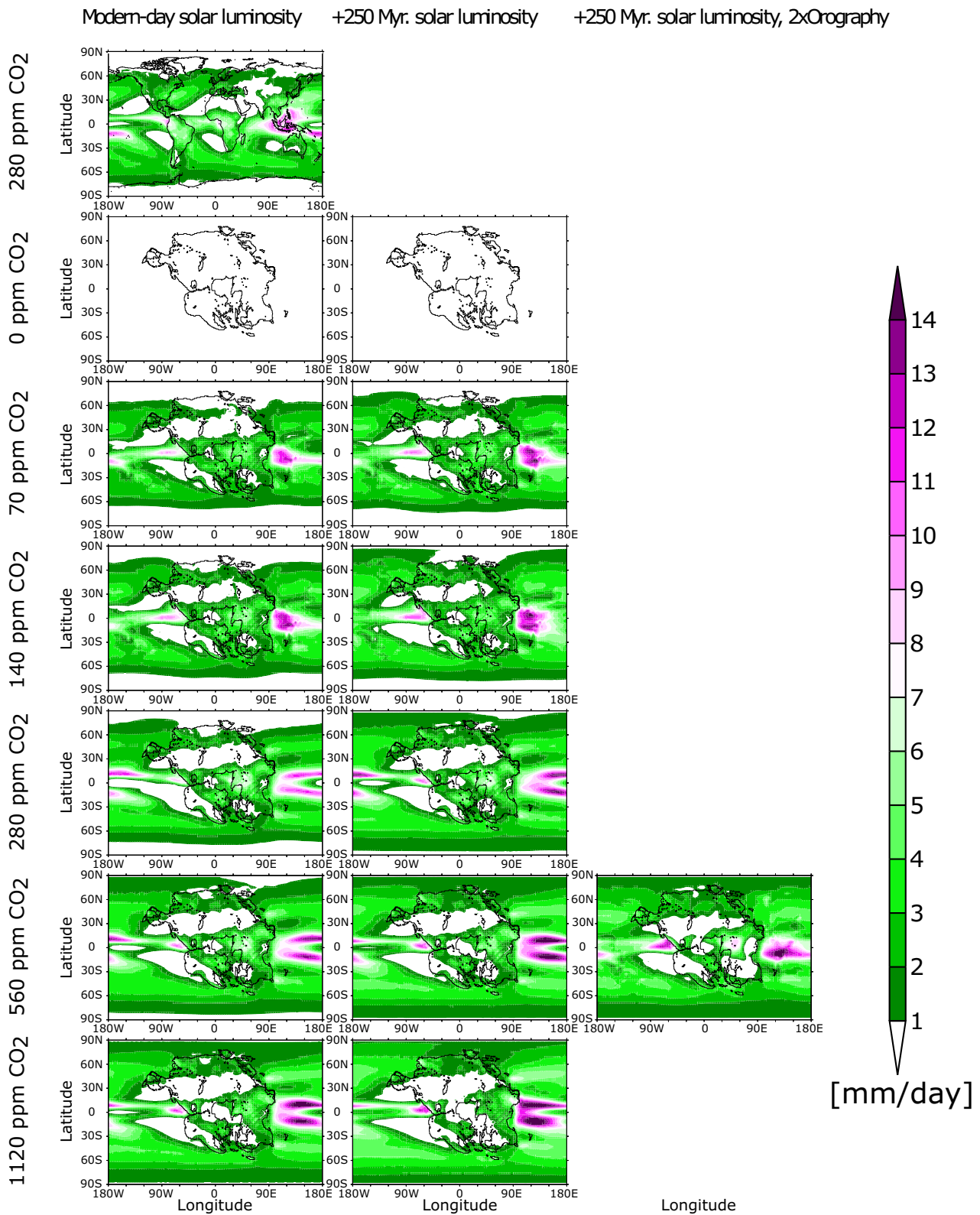 solar luminosity with a doubling of the topography (column 3) at 0 pm, 70 pm, 140 pm, 560 pm and 1120 pm CO2. Green = habitable area. Beige = fails heat stress metrics. Blues = fails cold stress metrics (see Methods). Red = Fails Heat stress metrics and is a (warm) desert.

Modern-day solar luminosity (F$_\odot$) **+250 Myr. solar luminosity (F$_\odot$)**

Extended Data Fig. 5 | Energy balance model analysis for each experiment relative to the pre-industrial experiment. Energy balance model analysis for each simulation relative to Pre-industrial control (280ppm CO2) simulation at present day (a,b,c; column 1) and +2.5% present day solar luminosity (d,e,f; column 2) at 280ppm, 560ppm and 1120ppm CO2.

Extended Data Fig. 6 | Energy balance model analysis for each experiment relative to the 280 ppm Pangea Ultima experiment. Energy balance model analysis for each simulation relative to Pangea Ultima 280ppm CO_2 simulation at present day (a,b,c; column 1) and +2.5% present day solar luminosity (d,e,f; column 2) at 280 pm, 560ppm and 1120ppm CO_2.

Extended Data Fig. 7 | Mean annual precipitation for each experiment. Mean annual precipitation (mm/day) for each experiment at present day (column 1), +2.5% present day solar luminosity (column 2) and +2.5% present day solar luminosity with a doubling of the topography (column 3) at 0 ppm, 70 ppm, 140 ppm, 560 pm and 1120 ppm CO2.